Journal of Solid State Chemistry **144,** 100–117 (1999)
Article ID jssc.1998.8125, available online at http://www.idealibrary.com on IDEAL®

Defect and Ordered Tungsten Oxides Encapsulated Inside 2H–WX_2 (X = S and Se) Fullerene-Related Structures

Jeremy Sloan,*,†,[1] John L. Hutchison,* Reshef Tenne,‡ Yishay Feldman,‡ Tatyana Tsirlina,‡ and Moshe Homyonfer‡

*Department of Materials, University of Oxford, Parks Road, Oxford, OX1 3PH, United Kingdom; †Inorganic Chemistry Laboratory, University of Oxford, South Parks Road, Oxford, OX1 3QR, United Kingdom; and ‡Department of Materials and Interfaces, Weizmann Institute, Rehovot 76100, Israel

Received July 21, 1998; in revised form December 2, 1998; accepted December 3, 1998

Complex tungsten oxides, consisting of nonstoichiometric oxides of the form WO_{3-x} and stoichiometric lamellar oxides of the form $\{001\}_R$ W_nO_{3n-1} ($n = 3$ to 6) have been observed incorporated within 2H–WX_2 (X = S or Se) inorganic fullerene-like (IF) structures by HRTEM. These encapsulates were formed from a gas–solid reaction between H_2X and disordered WO_{3-x} precursors exhibiting a range of particle sizes and morphologies. The microstructures of most of the encapsulated oxides could be described in terms of $\{hkl\}_R$ crystallographic shear (CS) structures formed relative to an ReO_3-type (R) substructure. Smaller spheroidal WO_{3-x} encapsulates were frequently found to exhibit random $\{103\}_R$ CS defects of the Wadsley type, while larger, needle encapsulates were found to form exclusively $\{001\}_R$ W_nO_{3n-1} type lamellar structures that were predominantely ordered. Spheriodal encapsulates with randomly spaced $\{001\}_R$ CS planes were also observed encapsulated inside 2H–WSe_2 IF structures. The growth and morphologies of the encapsulating 2H–WX_2 shells were profoundly influenced by those of the precursor oxides used in their formation. Ordering mechanisms were proposed with respect to the formation of the ordered encapsulated oxides from the disordered precursors. © 1999 Academic Press

1. INTRODUCTION

The encapsulation of reduced MO_3 (M = W and Mo) oxides inside defect layered chalcogenides of the form 2H–MX_2 is now well documented (1–4). The encapsulating 2H–MX_2 networks have been described as inorganic fullerene-related structures (IFs) because of their close resemblance to other fullerene-derived structures such as carbon nanotubes and nanoparticles. These similarities arise as a result of comparable behavior exhibited by both the structure of graphitic carbon (Fig. 1a) and the layered 2H–MX_2 structure (Fig. 1b). Under certain conditions of formation, both structures can incorporate defects in the form of non-six-membered rings (Figs. 1c and 1d) that cause either positive or negative curvature in the host lattices, resulting ultimately in the formation of either single-layered or multi-layered closed structures (5–7). Such structural modifications can lead to desirable physical properties and the 2H–MX_2 IFs have already found potential uses as solid lubricants (8), as tips for scanning probe microscopy (9), and as photovoltaic films (9). The two-dimensional 2H–MX_2 layered chalcogenides are also known to be useful in many applications, including their use in sliding electrical contacts (10) and as hydrodesulfurisation catalysts (11). It is anticipated that these applications and many others can be extended to their three-dimenisional 2H–MX_2 IF counterparts.

For IF-encapsulated oxides, the encapsulating 2H–MX_2 structures form by reaction of partially reduced MO_3 with gaseous H_2X according to the general mechanism depicted in Figs. 2a–2d (12). In the scheme, finely divided metal oxide particles (Fig. 2a) are partially reduced to give oxide precursor particles of uncertain stoichiometry (Fig. 2b) that are subsequently reacted with H_2X, and the encapsulating 2H–MX_2 "skin" then grows inward by progressive consumption of the outer surfaces of the oxide cores. The end products are empty nested IFs (Fig. 2d) and the encapsulated oxide cores (Fig. 2c) are therefore part of an intermediate product. The number of observed 2H–MX_2 encapsulating layers[2] depends on the extent of reaction of the oxide cores with H_2X and also on the particle size of the oxide precursors leading to their formation. What is currently not well understood is the precise nature of the encapsulated oxide cores and the relationships between

[1]To whom correspondence should be addressed. E-mail: jeremy.sloan@chem.ox.ac.uk.

[2]It is important to note here that 2H–MX_2 "layers" may incorporate both multiples and fractions of the contents of a unit cell with respect to the parent structure. For example, the 2H–WS_2 unit cell incorporates a total of four staggered hexagonal W atomic layers alternating with pairs of two staggered hexagonal S layers (Fig. 1b). Some IFs may incorporate odd numbers of these layers.

0022-4596/99 $30.00

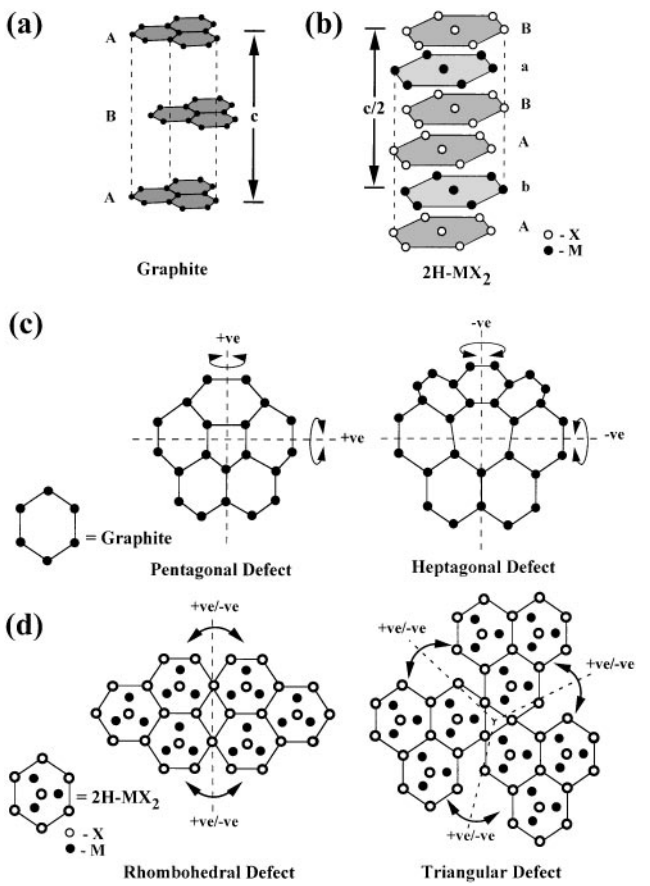

FIG. 1. (a) Graphite structure in perspective, showing … ABA … stacking sequence. (a) 2H–MX_2 structure in perspective, showing the more complex but structurally analogous … aBAbABa … stacking sequence. Note that only half the unit cell contents along c are shown and IFs with odd numbers of layers may incorporate such subunits of this structure. (c) Schematic diagram showing how incorporation of 5- and 7-membered rings cause positive and negative curvature in a graphitic lattice. (d) Schematic diagram showing how the incorporation of 3- or 4-membered rings can cause positive curvature in a 2H–MX_2-type lattice. Although direct evidence is lacking for other defects in the 2H–MX_2 cage structures such as the pentagonal or heptagonal defects depicted in (c) for carbon, they could be envisaged and indirect evidence for their prevalence exists.

their microstructures and the growth mechanism of the encapsulating 2H–MX_2 cages. Previously, average compositions of the encapsulated oxides have been determined, from bulk specimens, by X-ray powder diffraction (XRD) to be MoO_2, in the case of the encapsulated molybdenum oxides, and either β-$WO_{2.90}$ ($W_{20}O_{58}$) or γ-$WO_{2.72}$ ($W_{18}O_{49}$), depending on the reducing conditions, in the case of the encapsulated tungsten oxides (12). However, as the particle sizes of the encapsulated materials are in the range 7–50 nm (9), the contribution to the growth behavior of the encapsulating 2H–MX_2 materials from defects in the encapsulated oxides could be considerable, especially in view of the fact that tungsten oxides in particular form a wide range of nonstoichiometric compositions between MO_3 and MO_2 (13–21). This paper therefore describes the first detailed microstructural study with respect to tungsten oxides incorporated inside 2H–WX_2 fullerene-related structures. The comparative morphologies and microstructures of the oxide precursor particles leading to their formation are described and possible ordering mechanisms for the encapsulates are described and discussed.

2. EXPERIMENTAL

The preparation of the 2H–WX_2 encapsulated tungsten oxides was achieved via the following two steps: (i) evaporation and growth of WO_{3-x} precursor oxides followed by (ii) annealing in a reducing atmosphere containing the sulfidizing or selenizing agent. The synthesis of the precursor oxides was accomplished by evaporation of a tungsten wire in the presence of water vapor in a modified bell jar evaporation apparatus, according to a procedure described previously (9). The morphology of the precursors could be varied between small, approximately spherical, oxide nanoparticles and oxide needles by careful control of the evaporation conditions (9). As will be seen in Section 3.3, control over precursor size and morphology played a critical role in determining the corresponding size and morphology of the resulting encapsulates. The relationships between the pumping speed in the bell jar apparatus and the size and morphology of the oxide precursors is described fully in Section 3.1.

The sulfidization step occurs by passing a mixture of forming gas (5%H_2/95%N_2) at the rate of 120 ml/min for 30 min together with H_2S(g) at a rate of 2–4 ml/min over a reactor boat containing the finely divided and reduced oxide particles held in the temperature range 820–850°C (12). Both this reaction and the selenization reaction, described below, were performed at ambient pressure (1 atm) and the relative partial pressures of the sulfidizing/selenizing media with respect to that of the reducing atmosphere were therefore proportional to the flow rates. For some of the precursors, the tungsten had been co-evaporated with water containing 10^{-2}–10^{-3} moles of NaCl in order to produce sodium-doped fullerenes (9). In the case of the 2H–WS_2 encapsulated specimens, the oxide precursors and resultant encapsulated products were all derived from these sodium-doped precursors. For the 2H–WSe_2 encapsulated oxides, a reduced commercially available WO_3 powder (BDH) was used as a precursor material instead. The material had particle sizes in the range 100–150 nm and was reduced and then encapsulated by 2H–WSe_2 using a similar procedure to that used for the preparation of the 2H–WS_2 encapsulates but substituting H_2Se gas for H_2S. This encapsulation was performed at the lower temperature of 760°C for 90 min with a flow rate of 120 ml/min for the forming gas and 2–4 ml/min for H_2Se, respectively (3, 22). Note that in this case, the reduction and selenization occur simultaneously.

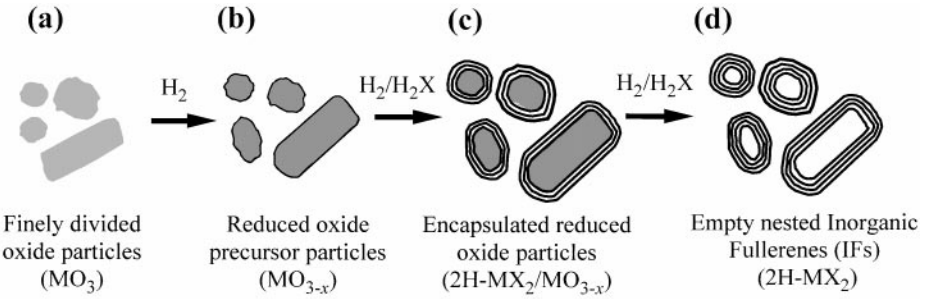

FIG. 2. General formation mechanism for 2H–MX_2 via a gas–solid reaction. Finely divided MO_3 oxide precursors of variable morphologies (a) are reduced to form reduced intermediates with MO_{3-x} stoichiometry (b) which are then reacted with H_2X gas to form partially encapsulated MO_{3-x} oxides (c) which, following complete reaction with H_2X, form hollow IF structures (d).

For high-resolution transmission electron microscopy (HRTEM) studies, the specimens were dispersed ultrasonically in ethanol before being placed dropwise onto lacy carbon coated specimen grids (Agar, Cu 200 mesh). The specimen grids were treated in a hydrophilic specimen cleaner (JEOL Datum HDT-400) to disperse residual oil contaminants that presumably originated from the bell jar pumping system. This procedure was not found to affect the specimens chemically in any way. Each specimen was characterized in a high-resolution (HRTEM) JEM-4000EX microscope operated at 400 kV (point resolution 0.17 nm). Electron diffraction (ED) patterns obtained from the various specimens and *d*-spacings were measured, to an accuracy of ± 0.005 nm, using a TlCl pattern as a reference standard. All high-resolution images were recorded at or close to optimum Scherzer defocus conditions. Because of the known tendency of a high-energy electron beam to induce defect formation and even crystal growth in tungsten oxides (21, 23–24), care was taken to minimize the amount of beam irradiation received by each specimen during lattice imaging. This was achieved by keeping the condenser aperture size to an optimal minimum and only exposing the crystals to a partially spread electron beam. For selected high-resolution images, HRTEM multislice image simulations were carried out using the EMS suite of programs (25) according to structural models described in the text. The microscope parameters used in these calculations are recorded in Table 1. Specimens formed in the presence of sodium were also characterized in a JEM-2010 microscope fitted with a LINK "Pentafet" energy dispersive X-ray microanalysis (EDX) system equipped with a windowless Si(Li) detector. A minimum probe diameter of 3 nm was utilized for all microanalyses.

TABLE 1
HRTEM Parameters for EMS Image Simulations

Accelerating voltage	400 kV
Spherical aberration coefficient (C_S)	0.9 nm
Semi-convergence angle (α)	0.8 mrad
Objective lens aperture diameter	10 nm^{-1}

3. RESULTS

3.1. HRTEM Characterisation of WO_{3-x} Precursor Oxides

As previously reported (9), the oxide precursor particles used to prepare the 2H–WS_2 oxide encapsulates were found to exhibit both variable particle sizes and morphologies that depended upon the pumping conditions used during their formation. These varied from: (I) small spherical or ellipsoidal particles with average diameters less than 20 nm (vacuum $\leq 10^{-2}$ Torr); (II) larger spherical or needle-like particles with diameters in the range 40–60 nm (vacuum 10^{-2}–10^{-3} Torr); and (III) oxide needles 50–100 nm in cross section and 500–2000 nm in longtitudinal dimensions (vacuum ca. 10–3 Torr). Some mixing of the three particle types was observed in all preparations although, for a given set of preparation conditions, predominance of one particular type was generally observed. The compositions of the precursor Types I–III were found by XPS to vary between $WO_{2.9}$ and $WO_{2.5}$ (9). Precursors formed by co-evaporation with sodium chloride were found, by the same technique, to contain up to a maximum of 8% Na, although these samples rarely contained more than 3% Na. XRD patterns obtained from bulk specimens indicated that all of the precursor particles were amorphous (9) but we now show, using a combination of ED and HRTEM imaging, that the precursor particles of Types I and II have disordered crystalline microstructures and that precursor oxide needles of Type III have highly disordered layered structures. ED patterns and HRTEM images revealed that the reduced commercially available oxide precursors had similar microstructures to particle Types I and II.

Figures 3a–3c show ED ring patterns obtained from groups of particle Types I and III and the reduced commercially available WO_3 precursor, respectively. While the patterns show some minor differences, the *d*-spacing

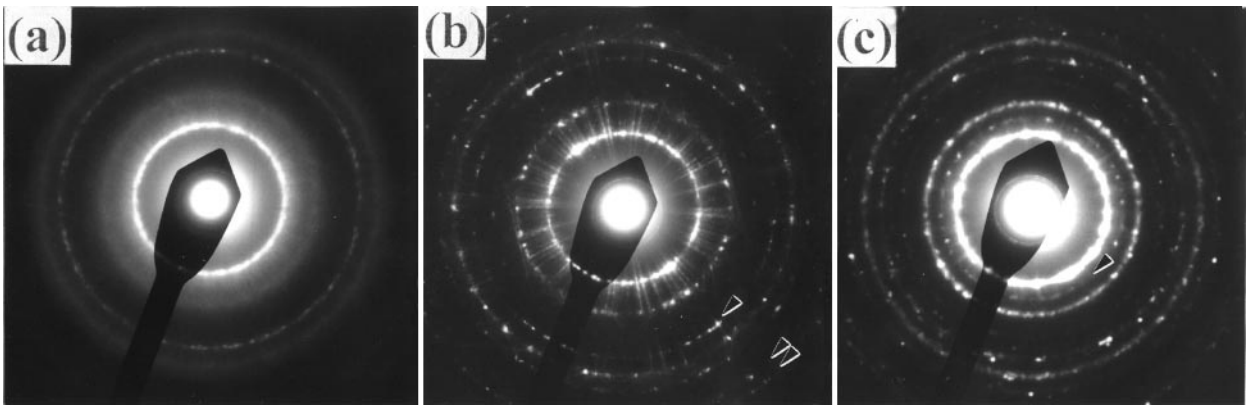

FIG. 3. (a) ED ring pattern obtained from a group of Type I precursor particles. (b) ED ring pattern, exhibiting diffuse radial streaking, obtained from a group of Type III precursor particle. Three additional reflections (arrowed) are visible relative to the pattern in (a). (c) ED ring pattern obtained from reduced commercially available precursor particles. One further reflection is visible relative to the pattern in (b).

information obtained from all of them corresponded closely to the tetragonal modification of $WO_{2.90}$ reported by Glemser *et al.* (26), but not to that reported for either the β- or γ-forms of tungsten oxide (27, 28). The calculated *d*-spacings of the three precursors and those reported for the tetragonal modification appear in Table 2. The latter, which was produced by thermal decomposition of $WO_{2.90} \cdot 2H_2O$, was indexed according to a cell with $a_0 = 0.53$ nm and $c_0 = 0.383$ nm (26). The main differences between the patterns in Figs. 3a–3c have to do with the number and type of reflections observed relative to the reported phase. The pattern obtained for particles of Type I (Fig. 3a) only exhibited five mainly diffuse reflections. The ring patterns produced by the Type III particles (Fig. 3b) exhibited three further reflections (arrowed) but also exhibited prominent radial streaking similar to that reported by Bonnet *et al.* for ring patterns obtained for $WO_{2.90}$ oxide needles produced by electron bombardment of WO_3 (24). Ring patterns obtained from Type II particles (not shown) were intermediate between those of Type I and Type III particles. Ring patterns obtained from the reduced commercially available WO_3 (Fig. 3c) exhibited one further prominent reflection (arrowed) but none of the radial streaking observed for the Type III particles (Fig. 3b).

HRTEM micrographs confirmed the microcrystalline nature of particle Types I–III and the reduced commercial

TABLE 2
Comparative *d*-Spacing Data for Tetragonal $WO_{2.90}$ (23), *d*-Spacings Obtained from ED Ring Pattern of Particle Types I/II, III and Reduced Commercially Available WO_3

Small particles (Type I/II)		Oxide needles (Type III)		Reduced commercial WO_3		Tetragonal $WO_{2.90}$ (25)		
Irel.	*d* (nm)	Irel.	*d* (nm)	Irel.	*d* (nm)	Irel.	*d* (nm)	*hkl*
100	0.374	100	0.375	100	0.374	100	0.374	110
—	—	—	—	30	0.306	20	0.310	101
40*d*	0.267	60	0.267	80	0.266	80	0.265	200
—	—	10	0.218	20	0.220	30	0.220	201
—	—	—	—	10	0.198	10	0.202	211
30	0.188	30	0.187	30	0.185	30	0.188	220
—	—	—	—	—	—	10	0.178	300
10*d*	0.163	40	0.165	50	0.166	60	0.167	310
10*d*	0.154	30	0.153	30	0.153	50	0.153	311
—	—	10	0.133	10	0.131	10	0.133	222
—	—	10	0.125	10	0.123	10	0.125	330
—	—	—	—	—	—	10	0.117	322

Note. *d*-Spacings were obtained from the experimental patterns with a TlCl pattern used as a reference standard.
*Intensities estimated visually, *d* denotes diffuse reflection.

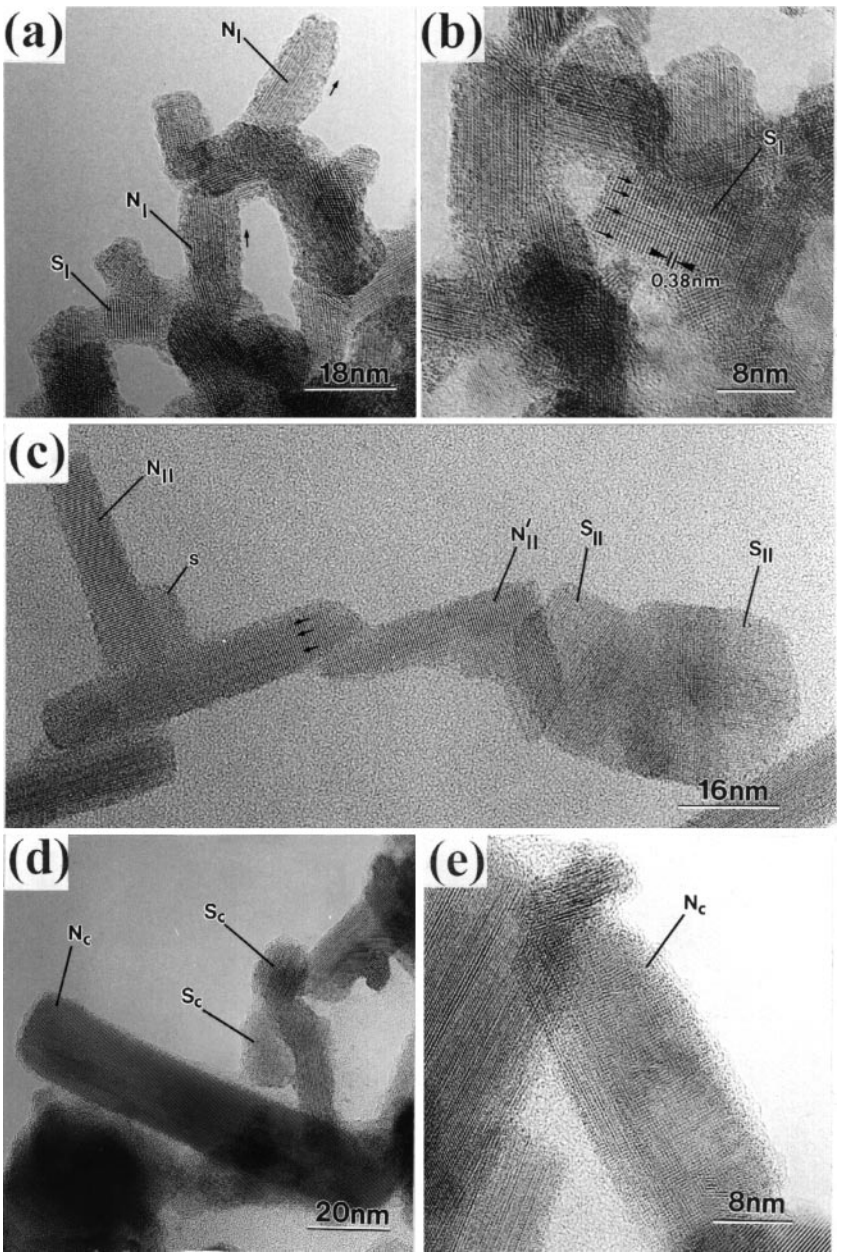

FIG. 4. (a) The Type I crystalline denoted $\mathbf{S_I}$ has a spherical morphology and exhibits prominent 0.38 nm or $\{100\}_R$ lattice fringes. The crystallites denoted $\mathbf{N_I}$ exhibit a tendency to grow along one preferred axis, as indicated by the small arrows. (b) The crystallite denoted $\mathbf{S_I}$ exhibits modulated $\{100\}_R$ lattice fringes, as indicated by the small arrows. (c) An "L"-shaped Type II crystallite, denoted $\mathbf{N_{II}}$, can be seen abutting onto a third Type II crystallite, denoted $\mathbf{N'_{II}}$. A step in the "leg" of this crystallite is denoted by **s**. Weak modulations of the $\{100\}_R$ lattice fringes (small arrows) are visible. Two overlapping spherical Type II crystallites (denoted $\mathbf{S_{II}}$) are also visible. (d) Needle-like ($\mathbf{N_C}$) and small spherical ($\mathbf{S_C}$) reduced commercially available precursor particles. (e) Disordered $\mathbf{N_C}$ precursor particles.

precursor. The micrograph in Fig. 4a was obtained from a group of Type I particles. The small spherical crystallite denoted $\mathbf{S_I}$ in Fig. 4a exhibits prominent 0.38 nm lattice fringes corresponding to $\{100\}$ layers of ReO_3-type WO_3 (29). These types of oxide layers shall henceforth be denoted $\{100\}_R$ layers, following the convention adopted by Miyano *et al.* (21). Several crystallites in the micrograph, denoted $\mathbf{N_I}$, exhibit a tendency to grow along one preferred direction, as indicated by the small arrows in Fig. 4a. Both $\mathbf{N_I}$ and $\mathbf{S_I}$ crystallites frequently exhibited modulated or disordered microstructures, presumably arising from their reduced state relative to WO_3. An example of this is shown for the $\mathbf{S_I}$

crystallite in Fig. 4b in which thin striations (arrowed) are clearly visible at 90° to the $\{100\}_R$ layers. Crystallites of Type II were found to exhibit both disordered microstructures and also more complex morphologies relative to the Type I crystallites. In Fig. 4c a Type II crystallite, denoted $\mathbf{N_{II}}$, shows that it is apparently dendritic in nature and consists of two short needle-like crystals growing at 90° to each other. This crystal abutts onto a second "L"-shaped crystallite, denoted $\mathbf{N'_{II}}$. Two "legs" of these "L"-shaped crystallites exhibit prominent steps (denoted **s**). Modulations of the $\{100\}_R$ layers of these crystallites are also visible (arrowed). Two disordered and overlapping spherical Type II crystals, denoted $\mathbf{S_{II}}$, are visible to the right of the two "L"-shaped crystallites. The reduced commercially available tungsten oxide particles were found to exhibit a range of particle sizes (ca. 5–30 nm) and morphologies spanning those exhibited by the Type I and Type II precursors. In Fig. 4d, two small spherical crystallites (denoted $\mathbf{S_C}$) and a needle-like crystallite (denoted $\mathbf{N_C}$) are both clearly visible. The larger crystallites were frequently disordered, as shown by the examples in Fig. 4e. In general, particles with spheroidal morphologies predominated in this specimen.

The as-grown Type III oxide needles were found by HRTEM to resemble oxide needles grown *in vacuo* by electron bombardment of WO_3 by Hashimoto *et al.* (30), Bonnet *et al.* (24), and Kumao *et al.* (31). In the latter two cases, the as-grown needles were attributed to the monoclinic form of β-$WO_{2.90}$ as described by Magnéli (27). The streaked ring patterns obtained from groups of the needles (Fig. 3b, above) were also similar to those obtained from groups of oxide needles by Bonnet *et al.* (24). ED patterns obtained from individual as-grown needles (Fig. 5a) resembled patterns obtained from individual needles by both Hashimoto *et al.* (30) and Bonnet *et al.* (24). These ED patterns consist of rows of diffraction spots spaced at distances corresponding to the 0.38 nm ReO_3-type substructure. The rows are smeared into diffuse streaks running normal to the needle axis (denoted **A** in Fig. 5a). Such diffraction behavior indicates a very high density of planar defects in the needles and inspection of the corresponding microstruc-

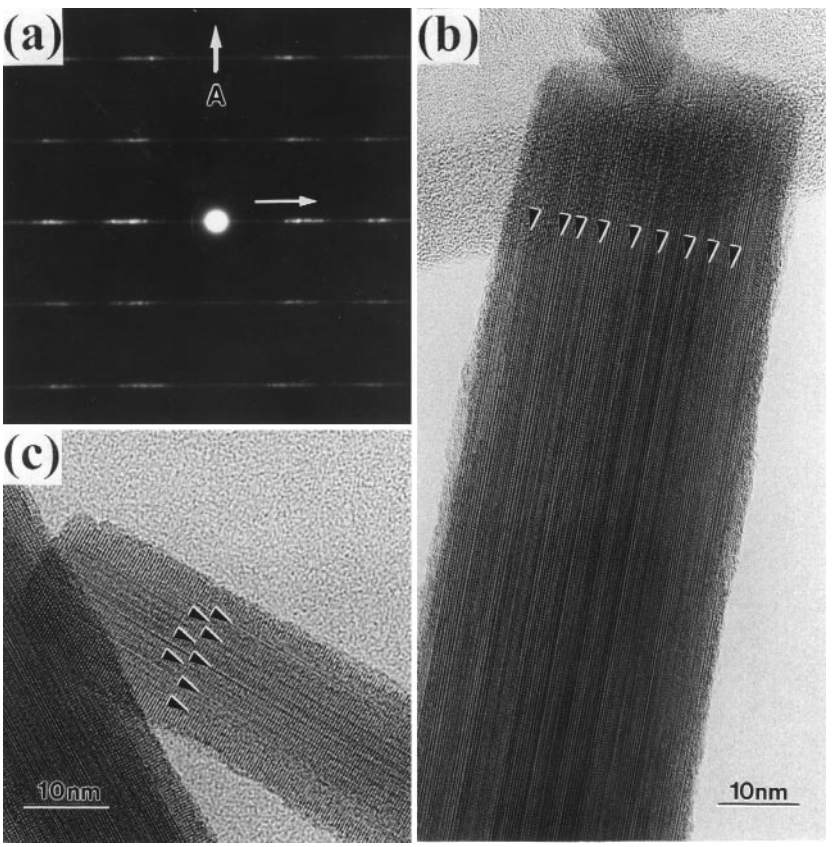

FIG. 5. (a) ED pattern obtained from an individual as-grown Type III precursor needle. The diffuse streaking along the central and parallel rows of reflections is at right angles to the needle axis. The inter-row spacing corresponds to the 0.38 nm repeat of the WO_3 sublattice (i.e., the $\{100\}_R$ layers). (b) Microstructure of needle giving rise to the ED pattern in (a). The microstructure is highly complex and no obvious layering sequence is visible parallel to the needle axis. (c) Micrograph obtained from a thin Type III needle. While some layering orthogonal to the $\{100\}_R$ layers is visible (arrowed), no overall ordering is discernible.

tures (Figs. 5b and 5c) reveals the source of the disorder as random layering (arrowed) occurring parallel to the needle axes. In thinner Type III needles (Fig. 5c), the source of the disorder is more visible but even these are not identifiably commensurate.

EDX spectra obtained from precursor particles of Types I–III indicated that smaller levels of Na (ca. 0.5–1.0%) were present in the precursors than had initially been indicated by XPS (3–8%). This discrepancy is possibly as a result of dispersal of Na by the electron probe. However, no significant contribution of Na to the oxide microstructures (e.g., as in bronze formation) was identified. While Na is clearly present in the precursors, at least at the dopant level, it is apparent that this species is not incorporated in any ordered fashion into the precursors. This conclusion is further supported by the observation that there are few significant differences between the diffraction behavior and microstructures of particle Types I, II, and III and those of the commercially available precursors in which no Na is present.

3.2. 2H–WS_2 Encapsulated Oxides

The 2H–WS_2 encapsulated oxides could be assigned to one of two general categories: small defect 2H–WS_2 encapsulates, formed from particle Types I and II; and 2H–WS_2 encapsulated oxide needles, formed from the Type III needle precursors. In terms of both morphology and microstructure, the smaller oxide encapsulates differed considerably from the larger needle encapsulates. While the smaller Type I and Type II particles formed small disordered oxide encapsulates, the Type III oxide needles formed ordered lamellar encapsulates that could generally be attributed to known tungsten oxide phases.

As with the oxide precursor particles, very low quantities of Na (ca. 0.5–1%) were detected in either the bulk of the oxide encapsulates or in the 2H–WS_2 walls via EDX. The assumption is again made here that Na does not contribute significantly to the microstructures of the encapsulates although it may well be present as a dopant, either in the walls of the 2H–WS_2 encapsulating material or in the encapsulated oxide crystals.

3.2.1. Small defect 2H–WS_2 encapsulates. In general, the smaller 2H–WS_2 encapsulates exhibited a range of sightly larger diameter (20–80 nm) than the oxide precursor particles giving rise to them (< 10–50 nm, see above). This expansion can be explained in terms of the greater cellular volume of 2H–WS_2 (0.1095 nm^3 (32)) relative to ReO_3-type WO_3 (ca. 0.0549 nm^3, based on $a_0 = 0.38$ nm). The external morphologies of the 2H–WX_2 encapsulates were found to be profoundly influenced by those of the oxide precursors giving rise to them. These were occasionally influenced by their own defect microstructures. An example of this type of structural bahavior can be seen in Fig. 6a. In the micrograph, a "bent" WO_{3-x} crystallite can be seen to be wholly encapsulated by the 2H–WS_2 network, visible as dark lattice 0.615 nm fringes corresponding to the (0002) planes of encapsulating 2H–WS_2 (32). The adjacent 0.38 nm $\{100\}_R$

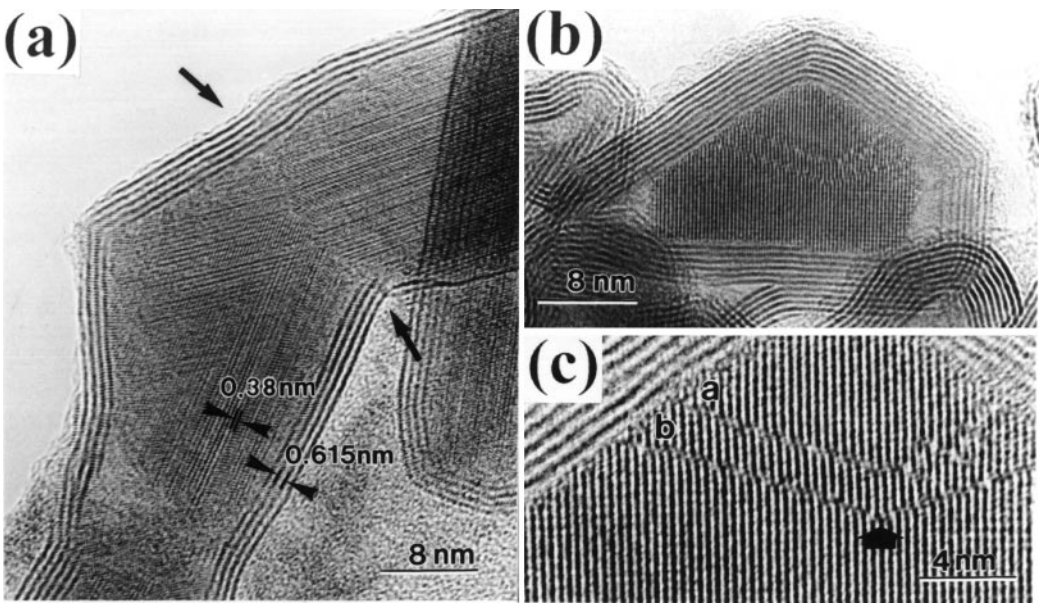

FIG. 6. (a) Micrograph showing how the external morphology of 2H–WS_2 encapsulate is influenced by the morphology and internal defect structure of the encapsulated oxide. The indicated 0.38 nm lattice fringes correspond to the $\{100\}_R$ layers of the encapsulated oxide. The arrows indicate the grain boundaries in the encapsulated oxide crystal that result in an overall 47.5° bend in both the crystallite and resulting encapsulate. (b) Small 2H–WS_2 defect encapsulate. (c) Enlargement of (b) showing the microstructure of the two CS-type defects (**a** and **b**).

WO_3 lattice fringes are clearly aligned parallel with respect to the encapsulating 2H–WS_2 layers. Inspection of the microstructure of the encapsulate reveals grain boundaries (arrowed) causing a 47.5° bend in the crystallite. The encapsulating 2H–WS_2 "skin" thus precisely follows the external morphology of the "bent" WO_{3-x} crystallite.

A significant number (10–20%) of the small oxide encapsulates were observed with defects formed as a result of crystallographic shear (CS). An example of a CS-type defect, originating from a Type I precursor particle, is shown in Fig. 6b. The micrograph shows a small oxide crystal encapsulated within eight (0002) layers of 2H–WS_2. The defect structure of the encapsulate is shown in enlargement in Fig. 6c. The prominent 0.38 nm lattice fringes again correspond to the $\{100\}_R$ planes of ReO_3-type WO_3. From left to right in the enlargement, two V-shaped defects (marked **a** and **b** in Fig. 6c) can be seen to extend from one internal face of the encapsulate to the other. On either side of the arrow in Fig. 6c, the direction of shear is reversed. Both CS planes are oriented at an angle of 20° with respect to the horizontal in Fig. 6c, suggesting that they are $\{103\}_R$-type (i.e., Wadsley type) CS planes as described by Bursill and Hyde (17).

A larger defect oxide encapsulate, presumably formed from an ellipsoidal Type II precursor particle, can be seen in Fig. 7a. In this micrograph, a 2H–WS_2 encapsulate with 18 randomly spaced $\{103\}_R$ CS defects can be seen. Toward the top of Fig. 7a a void (denoted **V**) resulting from partial consumption of the oxide core can also be seen. Visible between the CS planes are the 0.38 nm $\{100\}_R$ lattice fringes of WO_3. An enlargement of a portion of the WO_{3-x}/WS_2 interface, together with a schematic depiction of the microstructure, are given in Figs. 7b and 7c, respectively. At the observed defocus, the "steps" in the enlarged CS planes correspond to groups of six edge-sharing octahedra, as represented in Fig. 7c. A number of other features exhibited by this encapsulate give some indications as to the growth mechanism of the encapsulating 2H–WS_2 layer. An enlargement from the lower left of Fig. 7a (Fig. 7d) shows a region of the oxide–sulfide interface where two WS_2 layers can be seen propagating along the $\{100\}_R$ layers of the oxide core. However, the shape of the encapsulate toward the upper part of the micrograph in Fig. 7a indicates that the propagation is not restricted to growth along the $\{100\}_R$ oxide layers but also occurs at angles of 20°, 25°, and 90° with respect to the $\{100\}_R$ layers, as indicated by the arrows in Fig. 7a. In

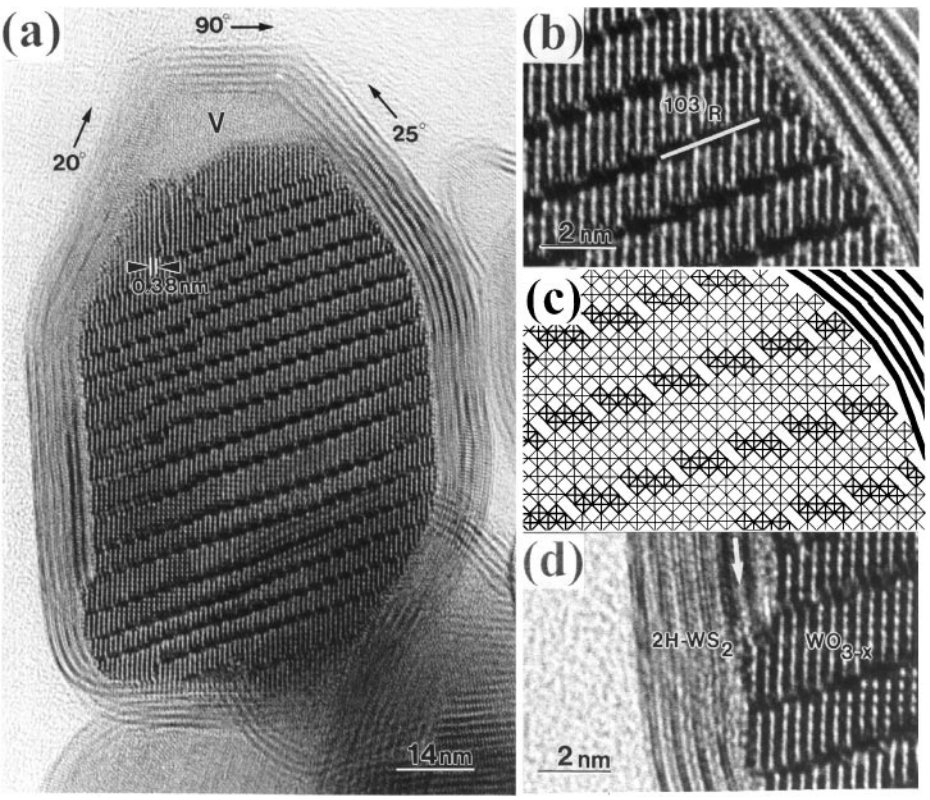

FIG. 7. (a) Large WO_{3-x} encapsulate with 18 $\{103\}_R$ Wadsley-type CS planes interspersed in an ReO_3-type WO_3 sublattice, indicated by the 0.38 nm $\{100\}_R$ lattice fringes. A void (**V**) is indicated at the top of the encapsulate. (b) Enlargement of WO_{3-x}/WS_2 interface. The prominent "step" in the $\{103\}_R$ shear planes correspond to the interfaces between the groups of six edge-sharing octahedra. (c) Schematic depiction of the WO_{3-x}/WS_2 interface as it appears in (b). (d) Enlargement of region in lower left of (a) showing propagation of two WS_2 layers along the $\{100\}_R$ WO_{3-x} layers.

this upper region, the growth of the 2H–WS_2 layer is apparently dictated by the adventitious morphology of the encapsulate rather than by propagation along the $\{100\}_R$ oxide layers.

A higher proportion of CS-type defect encapsulates similar to those observed in Fig. 6b and 7a is probably present in the specimen than actually observed (ca. 10–20%, see above) as the CS planes of many of the randomly orientated encapsulates may not be orientated parallel to the electron beam. All of the defect encapsulates that were observed were at or close to the correct orientation for the CS planes to be imaged and a minimum of "tilting" in the HRTEM was therefore required.

3.2.2. WS_2-encapsulated lamellar oxide needles. The 2H–WS_2 needle encapsulates exhibited similar dimensions to the Type III precursor needles from which they were formed (see Section 3.1). In Fig. 8a, the dimensions of an entirely encapsulated needle, situated among some smaller interspersed oxide encapsulates, can be seen. In Fig. 8b an enlargement of the microstructure of the encapsulated needle at one tip is shown. The thickness of the encapsulating sulfide layers varied from one encapsulate to another, but was generally in the range 2–8 2H–WS_2 layers per encapsulate. Tilting of the encapsulated needles about their axes (indicated by **A** for the example in Fig. 8b) did not usually reveal any breaks in the 2H–WS_2 coverage, indicating that it was complete in most cases. The needle in Fig. 8b can be seen to be wholly 2H–WS_2 encapsulated although the coverage is clearly asymmetric. In the given example, the tip is coated with four 2H–WS_2 layers, while the two longitudinal faces are coated with four 2H–WS_2 layers and two 2H–WS_2 layers, respectively, suggesting a "scrolling" growth mechanism for the encapsulating network as it formed around the needle. A further point is that any variations in the external morphology of the needle encapsulates were followed by the encapsulating material. In Fig. 8b a small step (denoted **s**) in the needle encapsulate is duplicated by the encapsulating layer (cf. Fig. 6a).

As with the smaller oxide encapsulates, progressive consumption of the needle oxide cores leads to void formation and an example of this is shown in Fig. 8c (cf. Fig. 7a). In this case, asymmetric consumption of the oxide core has led to the formation of a longitudinal void (denoted **V** in Fig. 8c) formed along the entire length of the encapsulate. It is

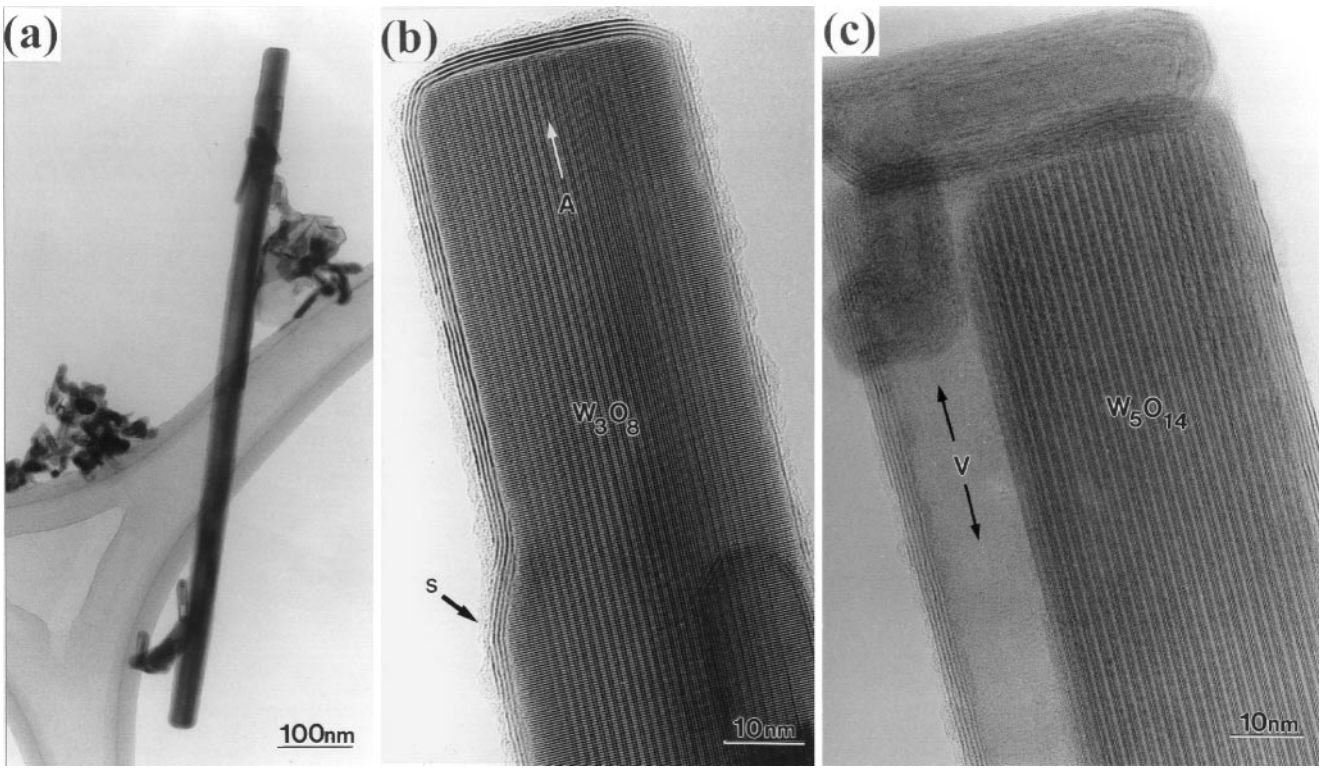

FIG. 8. (a) Micrograph of a wholly 2H–WS_2 encapsulated tungsten oxide single crystal. Smaller oxide encapsulates are also visible in the micrograph. (b) Enlargement of tip of needle in (a) showing asymmetric coverage of needle tip by encapsulating 2H–WS_2 layers. Tilting of this needle about the axis **A** did not reveal any break in the 2H–WS_2 coverage, despite the asymmetry. A small step in the oxide needle (denoted **s** in the micrograph) is followed by the encapsulating layer. The ordered microstructure of this $n = 4$ needle is further enlarged in Fig. 9b. (c) Micrograph showing continuous longitudinal void (denoted **V**) formed by partial consumption of an $n = 5$ needle core. Note that the 2H–WS_2 capsule retains its structural integrity. Smaller oxide encapsulates can be seen adhering to the tip of this encapsulate.

noteworthy that, despite formation of this void, the structural integrity of the encapsulating 2H–WS_2 network is retained and completion of the sulfidization process would presumably lead to the formation of a rigid 2H–WS_2 nanotube of similar dimensions to the needle from which it originated.

One of the most significant features concerning the encapsulated oxide needles is that nearly all had formed ordered microstructures in contrast to those of the precursor oxide needles from which they were formed. The absence of any disorder in most of the needle encapsulates was demonstrated by HRTEM lattice images and furthermore by the absence of streaking in their corresponding ED patterns (cf. Fig. 5a). The ordered lamellar encapsulates conformed to a $\{001\}_R$ W_nO_{3n-1} homologous series of layered phases previously described by Miyano *et al.* (21). These reported structures, which were formed by electron beam irradiation of vacuum deposited WO_3 films, were defined in terms of ordered $\{001\}_R$ CS planes demarcating n layers of corner sharing WO_3 octahedra (21).

In Figs. 9a and 9b, [010] and [100] projections of encapsulated needles corresponding to the $n = 6$ homologue of the W_nO_{3n-1} homologous series (i.e., W_6O_{17}) can be seen, together with their corresponding inset indexed ED patterns. The microstructures in both projections are represented in Fig. 9c and 9d, respectively. Evident in Fig. 9a is, first of all, the [100] shearing of the structure and, second, the monoclinic symmetry common to all the observed W_nO_{3n-1} encapsulated needles. This presumably originates from distortions inherent in the oxide sublattice as strict adherence to either a cubic or tetragonal ReO_3-type subcell would result in, respectively, tetragonal or orthorhombic symmetry, by inspection. The inset simulated images in Figs. 10a and 10b were calculated based on [010] and [100] projections of the structural models as depicted in Figs. 10c and 10d, respectively, with the monoclinic space group *Pm* (No. 6) and the lattice parameters $a_0 = 0.38$ nm, $b_0 = 0.38$ nm, $c_0 = 1.8$ nm, and $\beta = 85^\circ$. The encapsulated and partially consumed encapsulated needle in Fig. 8c is an example of an $n = 5$ encapsulate homologue from the same series viewed, in this case, along [010].

The microstructure of the encapsulate shown in Fig. 10a is enlarged from Fig. 8b and corresponds to a projection along [100] of an $n = 3$ member of the W_nO_{3n-1} homologous series. The ordered nature of this needle is apparent both from the microstructure and also the inset electron diffraction patters (cf. Fig. 5a). An image simulation based on the structural model in Fig. 10c with the same space group as above and the lattice parameters $a_0 = 0.38$ nm, $b_0 = 0.38$ nm, $c_0 = 1.1$ nm, and $\beta = 85^\circ$ provides good agreement with the observed image contrast. In Fig. 10b, a [010] projection of an encapsulated $n = 4$ needle (enlarged from Fig. 8b) can be seen. While this encapsulate obviously has a lamellar microstructure, it is not sheared in the same way as the $n = 6$ homologue described above. Inspection of the image contrast at a glancing angle along the direction indicated by the dark arrow in Fig. 10b reveals the lack of overall shear (i.e., adjacent layers are not staggered—cf. Fig. 9a) although the presence of strain in the crystal is evident from the monoclinic distortion. Image simulation studies suggest that this encapsulate is possibly in a highly strained "pre-shear" state with the loci of the shear planes being occupied instead by partial vacancy walls, as depicted in Fig. 10d. An inset image simulation in Fig. 10b based on this model (with $a_0 = b_0 = 0.38$ nm, $c_0 = 1.3$ nm, and $\beta = 85^\circ$) provides a reasonable match with the observed image contrast. Such a precursor stage has already been proposed by Miyano *et al.* for the formation of W_4O_{11} based on HRTEM images obtained from the [100] projection rather than [010] (21). It is noteworthy that the $n = 3$ microstructure is apparently slightly expanded, having almost the same lattice parameter as the $n = 4$ microstructure. We will comment further on the phenomenon of CS plane formation and the $n = 3$ structural expansion in the discussion.

A small percentage ($< 5\%$) of the observed oxide needle encapsulates exhibited only partial ordering, as shown by the example in Fig. 11a. Closer inspection of the microstructure of the oxide encapsulate in Fig. 11b, which is enlarged from the region to the right of the arrow in Fig. 11a, reveals that it consists of an WO_3 oxide sublattice interspersed with diffuse contrast modulations, arrowed in Fig. 11b, superimposed on the ordinary image contrast. These very weak contrast modulations again suggest oxygen vacancy wall formation rather than CS plane formation (see subsequent discussion). The corresponding ED pattern, inset into Fig. 11a, exhibits prominent streaking along the lattice direction corresponding to the disorder. These lateral streaks are interspersed with weak incommensurately spaced superlattice reflections (arrowed) that are distinct from more prominent reflections corresponding to the oxide sublattice. In the enlargement of the microstructure (Fig. 11b), the weak superimposed fringes (arrowed) can be seen to be incommensurately spaced with respect to the substructure, suggesting the nature of the discommensuration in real space. Toward the right of Fig. 11b, the superimposed dark fringes apparently disappear and an ordered ReO_3-type WO_3 substructure, exhibiting a slight tetragonal distortion, is observed.

3.3. *2H–WSe_2 Incorporation of Disordered W_nO_{3n-1} Layered Structures*

All of the 2H–WSe_2 encapsulates were produced from the reduced commercially available WO_3 powder, as described in Section 2. CS structures similar to those described above for the small defect encapsulates (Section 3.2.1) were observed although these were fewer in number than those

observed for the 2H–WS_2 encapsulates. As the reaction of H_2Se with the oxide was carried out over a longer time scale, thicker walled encapsulates (10–20 IF layers) were obtained compared to those described above for the 2H–WS_2 encapsulates (4–10 IF layers). In addition, the observed encapsulates were mainly spherical in nature and no needle-like encapsulates were observed. However, as smaller oxide precursor particles were used in the formation of the 2H–WSe_2 encapsulates, this result is to be expected.

Figure 12a shows an example of a 2H–WSe_2 encapsulated CS structure. The dark 0.65 nm lattice fringes of the material surrounding the encapsulate this time represent the

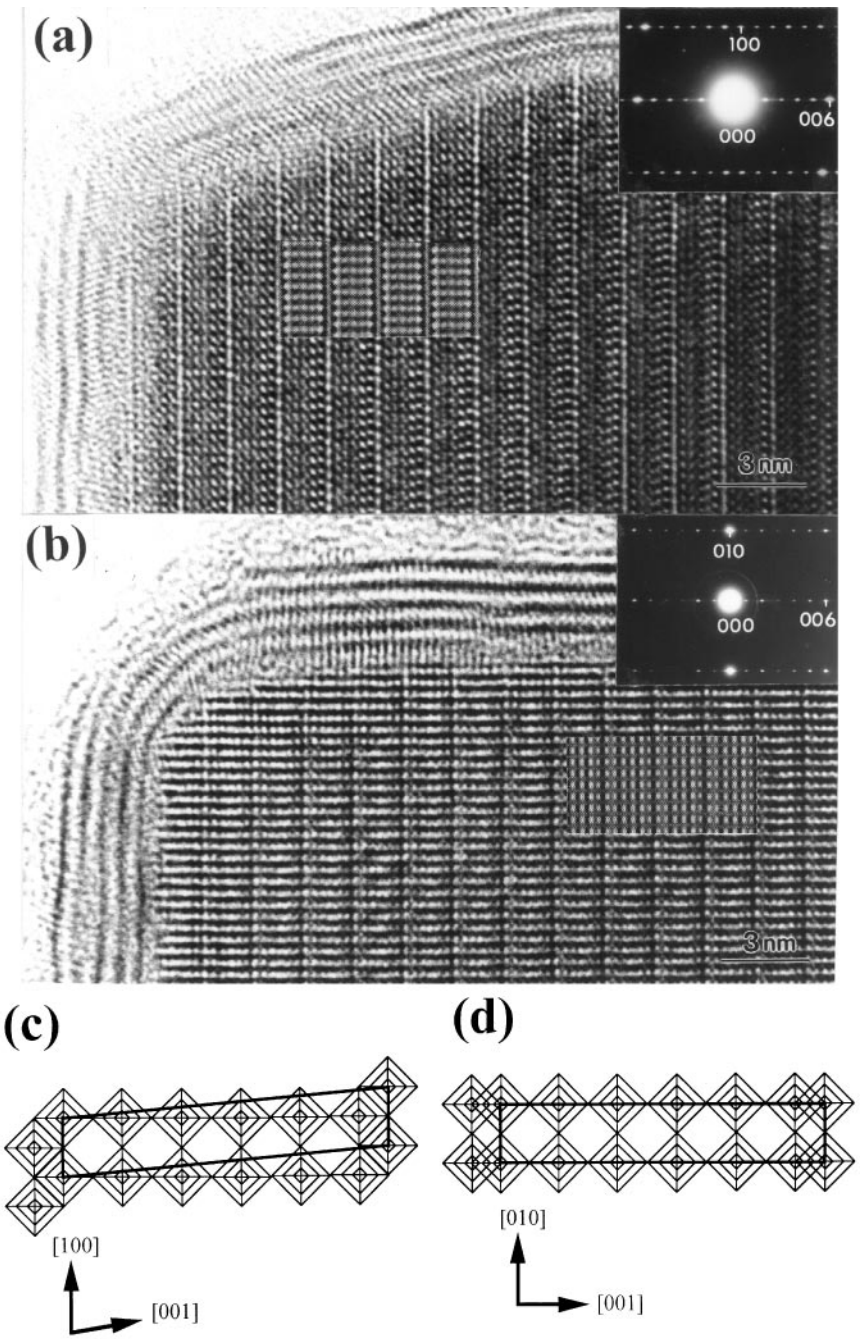

FIG. 9. (a) Lattice image, inset ED pattern, and computed simulated image obtained for an [010] projection of an 2H–WS_2 encapsulated W_6O_{17} needle. The inset simulated image was computed for an 1.5 nm thick foil at 80 nm underfocus. (b) As for (a) but in [100] projection. The inset simulated image was computed for an 1.6 nm thick foil at 90 nm defocus. (c) Schematic representation of W_6O_{17} in [010] projection. (d) Schematic representation of W_6O_{17} in [100] projection.

(0002) planes of the encapsulating 2H–WSe_2 network (33). At low magnification, the CS planes are clearly visible as dark straight lines interspersed at irregular intervals throughout the encapsulated oxide. At higher magnification, in Fig. 12b, the 0.268 nm lattice fringes of the WO_3 sublattice can be seen to be orientated at an angle of ca. 47° to the CS planes. At this image defocus, these lattice fringes correspond to the $\{110\}_R$ planes of the WO_3 sublattice. The

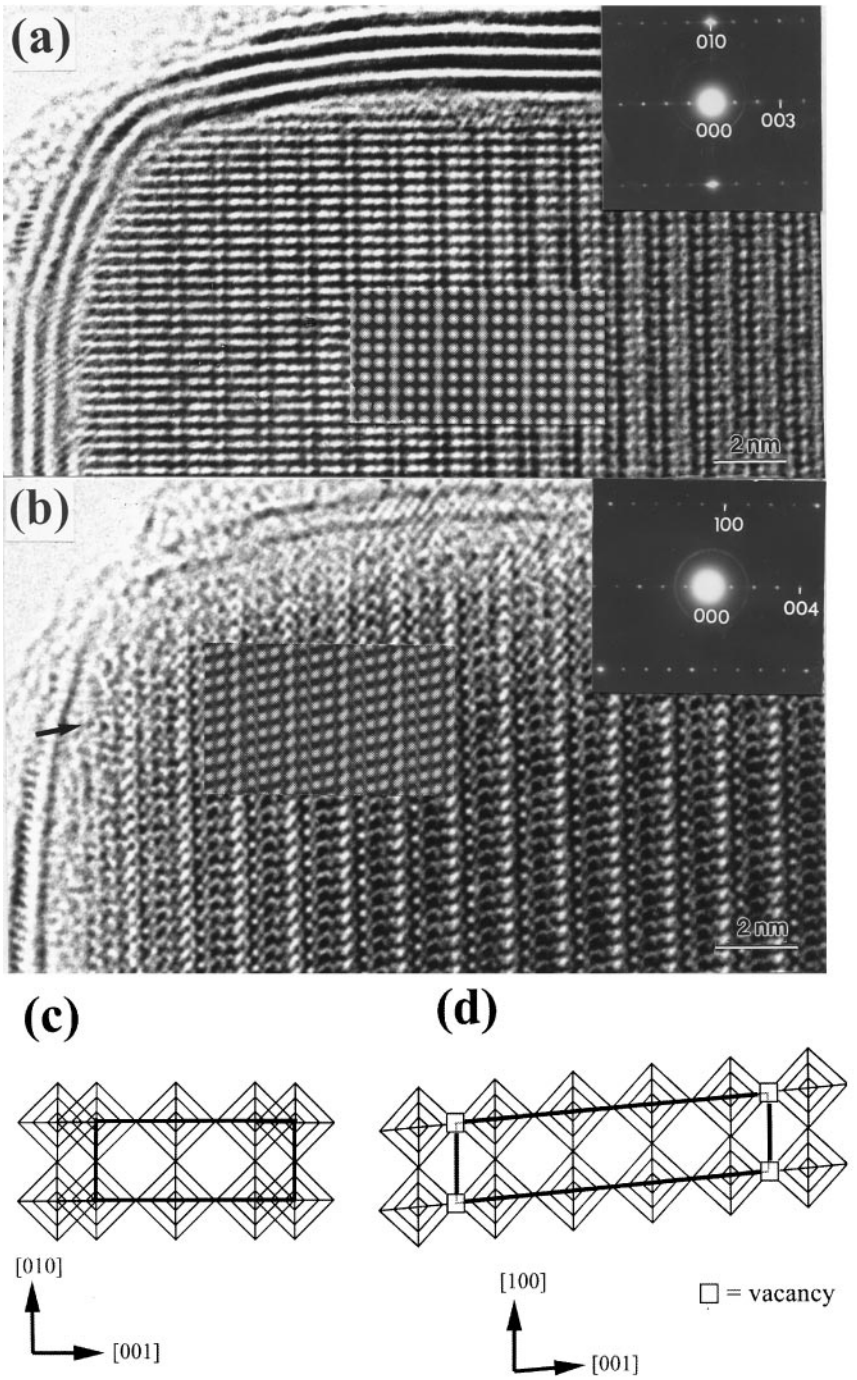

FIG. 10. (a) Lattice image (enlarged from Fig. 8b), inset ED pattern, and inset simulated image corresponding to a [100] projection of a 2H–WS_2 encapsulated W_3O_8 needle. The simulated image was computed for a 1.5 nm thick foil at −98 nm defocus. (b) Lattice image, inset ED pattern and inset simulated image corresponding to an [010] projection of the W_4O_{11} partial shear structure. The absence of full shear may be seen by viewing the microstructure at a glancing angle along the direction indicated by the arrow. The simulated image was computed for a 1.5 nm thick foils at −50 nm defocus. (c) and (d) are schematic representations of the microstructures in (a) and (b), respectively.

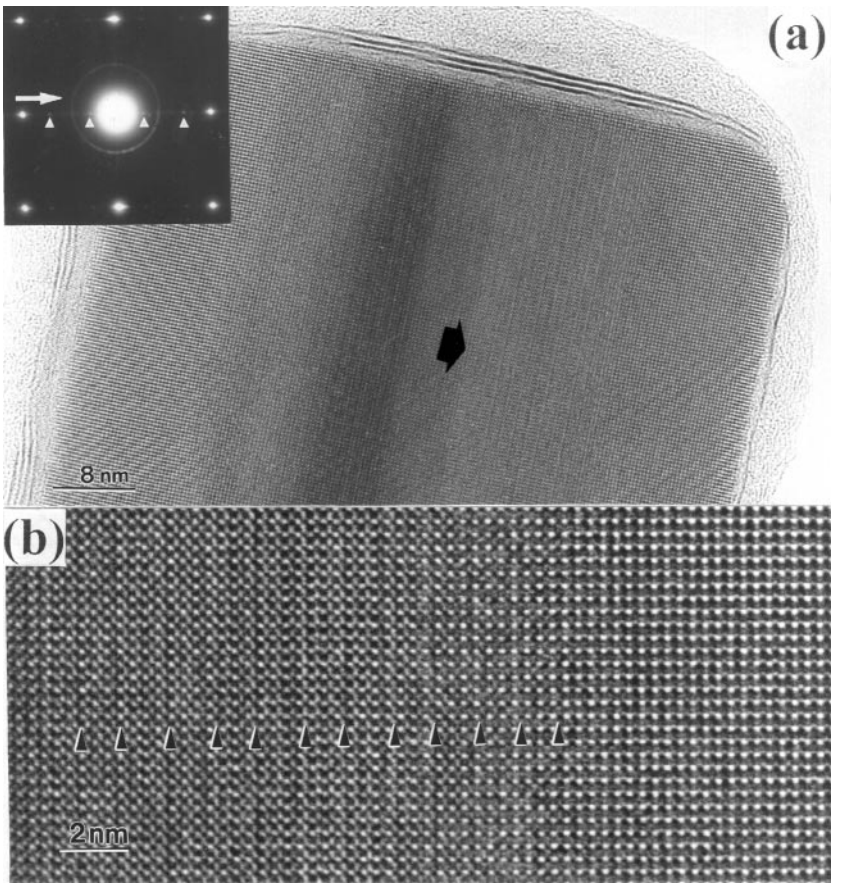

FIG. 11. (a) Micrograph and inset diffraction pattern obtained from an incommensurate WO_{3-x} needle encapsulate. The strong reflections in the ED pattern indicate a pronounced ReO_3-type subcell while weaker streaked incommensurate reflections (arrowed) indicate the superimposed partial ordering. Note that these reflections are incommensurate with respect to those of the subcell. The ring in the ED pattern is an artifact. (b) Enlargement of microstructure from right of arrow in (a) showing diffuse incommensurately spaced contrast modulations (arrowed) interspersed in the WO_3 sublattice which disappear towards the right of the enlargement.

observed CS planes are therefore randomly dispersed $\{001\}_R$ CS planes, as described above for the ordered W_nO_{3n-1} encapsulates, and not $\{103\}_R$-type CS planes. The higher magnification image in Fig. 12b reveals that these CS planes are randomly distributed throughout the encapsulated WO_3 matrix. No fully ordered encapsulates have yet been observed for the 2H–WSe_2 encapsulates as described above for the 2H–WS_2 encapsulates. The lack of ordering in the 2H–WSe_2 encapsulates can possibly be attributed to the lower temperature of encapsulation.

4. DISCUSSION AND CONCLUSIONS

4.1. Microstructures and Morphologies of Oxide Precursors

Despite their differing conditions of formation, all four precursors described in Section 3.1 exhibited ED ring patterns that could be correlated with the diffraction behavior reported for $WO_{2.90}$, that is, the tetragonal modification of ReO_3-type WO_3 (21). However, the HRTEM images obtained from all of the precursors (Figs. 3–5) suggest that this simple structure is probably inadequate in terms of the overall characterization of the precursors. Furthermore, the ED patterns and microstructures of these materials are inconsistent with those of either of the commonly cited tungsten oxides, namely β-$WO_{2.90}$, which consists of ordered $\{103\}_R$ shear planes interspersed in a distorted ReO_3-type structure (14), or γ-$WO_{2.72}$, which consists of ordered pentagonal columns (PCs) similarly dispersed in an ReO_3-type structure (34). In view of the observation that, upon encapsulation, the precursors order to form partially or fully ordered encapsulated oxides, a more complete understanding of their microstructural behavior may be considered to be essential.

One of the most important aspects of precursor formation concerns the relationship between their morphology and microstructure. At the lower ranges of particle sizes (Type

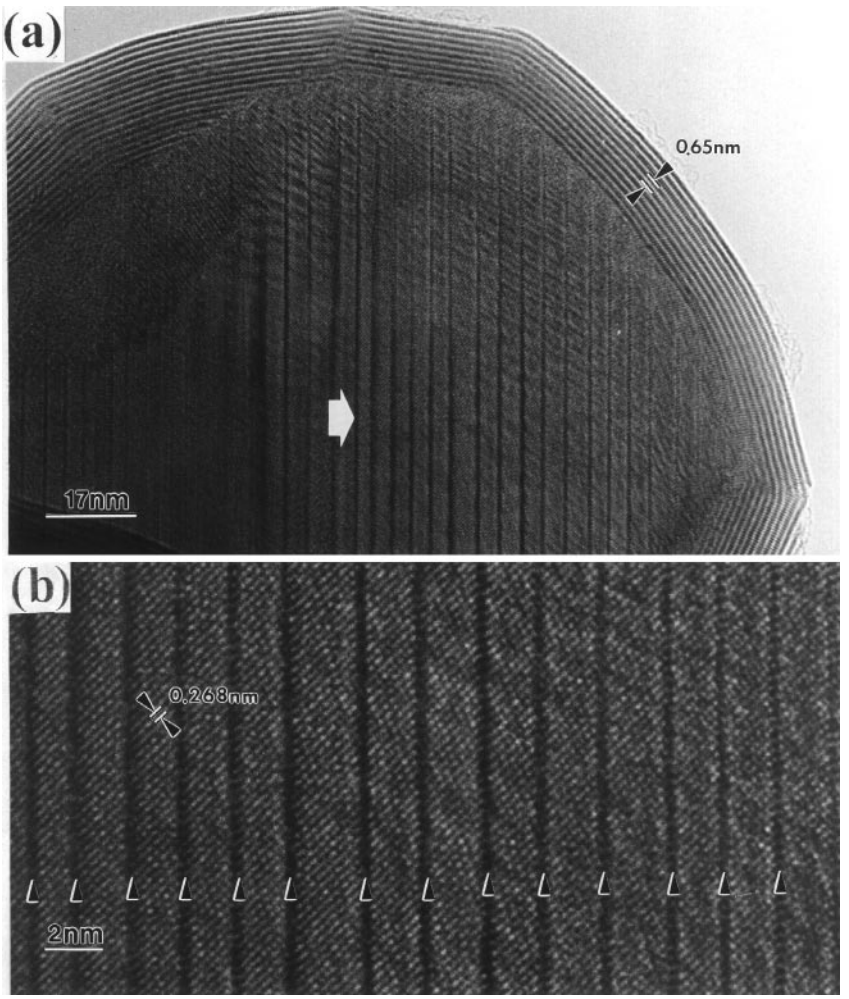

FIG. 12. (a) Micrograph showing 2H–WSe_2 encapsulated oxide with randomly spaced $\{001\}_R$ CS planes. (b) Enlargement of microstructure in (a). At this magnification, the 0.268 nm lattice fringes corresponding to the $\{110\}_R$ planes of WO_3 sublattice are clearly visible. Note the linear nature of the randomly spaced CS planes (cf. Fig. 7a–7c).

I and II) spheroidal ($\mathbf{S_I}$ and $\mathbf{S_{II}}$) particles co-existed with elongated needle-like particles ($\mathbf{N_I}$ and $\mathbf{N_{II}}$) (see Figs. 4a–4c). The largest particles (Type III) were found to exhibit exclusively needle-like morphologies (Figs. 5b and 5c). Regardless of their morphologies, all of the precursors apparently exhibit the same ReO_3-type substructure, visible in the HRTEM as 0.38 nm lattice fringes (identified as the $\{100\}_R$ layers) and in the ED patterns as the ReO_3-type subcell. As the particle size of the precursors was increased, disorder in the form of contrast modulations occurring at 90° to the substructure $\{100\}_R$ layers was observed that was most pronounced for the largest Type III precursors. In the case of the latter, this disorder was also manifested in ED patterns that exhibited either radial streaking, in the case of ring patterns obtained from groups of needles (Fig. 3b), or linear streaking, in the case of patterns obtained from individual needles (Fig. 5a). The disorder observed in the lattice images obtained from the needles was so profound that it was difficult to identify any overall structure (e.g., Fig. 5b).

If we accept an ReO_3-type substructure for the precursors, then two closely related structural elements may possibly contribute to the observed disorder. The first, already clearly identified as a structural feature in the products, are randomly distributed $\{001\}_R$ CS planes formed orthogonal to the $\{100\}_R$ planes of the oxide sublattice. A single $\{001\}_R$ CS plane, formed in an undistorted WO_3 sublattice, is depicted schematically in Fig. 13a. The second element, depicted in Fig. 13b, consists of partial oxygen vacancy walls (PVWs), which are comprised of random oxygen vacancies formed in rows of linking oxygen sites shared by rows of corner sharing WO_3 octahedra. The formation of $\{103\}_R$ PVWs were originally proposed by Gadó (35) as the precursor stage to the formation of $\{103\}_R$ CS planes. Their formation *in situ* was demonstrated by Iijima (23),

for the formation of $\{102\}_R$ and $\{103\}_R$ CS planes, and subsequently by Miyano *et al.* (21), for the formation of $\{001\}_R$ CS planes. In all three cases, the PVW formation was induced by electron bombardment of WO_3 in a HRTEM and was characterized in terms of diffuse dark bands that appeared in the crystals prior to CS plane formation. These were attributed to localized strain fields induced by the production of oxygen vacancy walls in the crystals.

If CS planes and PVWs are the only two elements contributing to the lamellar disorder observed in the precursors, then three possibly overall structural configurations can be countenanced. The first, depicted in Fig. 13c, consists of a WO_3 substructure interspersed with randomly distributed $\{001\}_R$ CS planes; the second, depicted in Fig. 13d, consists of an WO_3 substructure interspersed with randomly distributed $\{001\}_R$ PVWs; and the third, depicted schematically in Fig. 13e, consists of an ReO_3-type lattice randomly interspersed with both $\{001\}_R$ CS planes and $\{001\}_R$ PVWs. None of these structural models is inconsistent with known tungsten oxide chemistry.

4.2. Proposed Mechanisms of Ordering of Precursor Oxides to Form 2H–WX_2 Encapsulates

Given the three possible structural configurations of the precursors described in the preceding section, it is possible to propose a number of mechanisms by which these proposed microstructures order to form the encapsulated microstructures encountered in this study. In order to be considered valid, the mechanisms described must fulfill the following criteria: (i) the net product is a structure with a thermodynamically favored and ordered (or partially ordered) configuration; (ii) the energetics of the mechanism must be consistent with the reaction conditions employed in the formation of the products. The only additional "degree of freedom" allowed with respect to the described mechanisms is the ability of the encapsulated oxides to undergo further reduction, and thereby additional CS plane or PVW formation, during the encapsulation process.

If the disordered precursors consist solely or randomly distributed $\{001\}_R$ CS planes (Fig. 13b), then ordering of the microstructures can proceed by one of two possible routes. The first route, depicted schematically in Fig. 14 by path $A \rightarrow C \rightarrow D$, involves ordering of $\{001\}_R$ CS planes by their migration to thermodynamically favorable loci. According to this mechanism, the $\{001\}_R$ CS planes unshear to form a structure with a full oxygen vacancy wall (FVW), in which all of the shared oxygen sites in an W–O–W interlayer are temporarily vacant, at the former locus of the $\{001\}_R$ CS plane (CS + FVW/PVW Intermediate I). The FVW then migrates to the thermodynamically favored locus, thus forming a second intermediate (CS + FVW/PVW Intermediate II) which then reshears to form the ordered product, in this case W_4O_{11}. Alternatively, the CS plane may migrate one octahedral row at a time, as indicated by pathway B(1) and B(2) in Fig. 14. According to this mechanism, as soon as one octahedral row unshears, the CS plane reforms with the adjacent octahedral row. This process continues until an ordered structure is achieved. The second possible mechanism involves the introduction of new $\{001\}_R$ CS planes at thermodynamically adventitious sites. According to the mechanism developed by Iijima and Gadó (23, 35) this stage must be presaged by the introduction of PVWs. Thus pathway D in Fig. 14 obtains in which PVWs, formed at a thermodynamically favored locus, shear to form the ordered product. This mechanism asssumes that the structure is already partially ordered and that the $\{001\}_R$ CS planes already present in the structure are disposed in such a way that introduction of further $\{001\}_R$ CS planes at the appropriate sites results in the formation of an ordered structure.

If the disordered precursors consist solely of randomly distributed PVWs (i.e., Fig. 13d), two mechanisms similar to those described above can obtain. First, the PVWs can migrate to thermodynamically favored loci whereupon they undergo the ordinary shearing process to produce an ordered array of $\{001\}_R$ CS planes in the product crystal (as for the PVW in pathway C, Fig. 14). Second, new PVWs can form at thermodynamically favorable positions determined by the pre-existing PVW configuration of the precursor crystal. These introduced CS planes and the stationary PVWs then undergo the ordinary shearing process to produce an ordered crystal (as for the PVW in pathway D, Fig. 14). If the disordered crystal consists of both randomly dispersed CS planes and PVWs, then the ordering mechanism can be described in terms of either PVW migration or CS plane migration. Additional shear planes may be introduced at adventitious sites to produce an overall ordered structure.

While these models have been described mainly from the point of view of lamellar structures with $\{001\}_R$-type defects, they can also be adapted to account for the formation of the $\{103\}_R$ CS encapsulates from the approximately spherical precursor particles. In case of the spherical precursors, the random CS planes or PVWs may be forming on planes other than $\{001\}_R$ which would account for the observation of the $\{103\}_R$ CS encapsulates (Fig. 7a). However, neither $\{103\}_R$ CS planes or PVWs were unambiguously identified in the precursors.

All of the proposed mechanisms described above have their merits and drawbacks. The least likely mechanism may be considered to be that involving ordering by CS plane migration. Apart from the unfavorable energetics of bond-making and bond-making, this mechanism must produce a net expansion for the CS plane as it unshears to form a FVW. This situation must be seen as unfavorable inside an IF which may not be able to accommodate the expansion. Once formed, however, the driving force for the FVW to

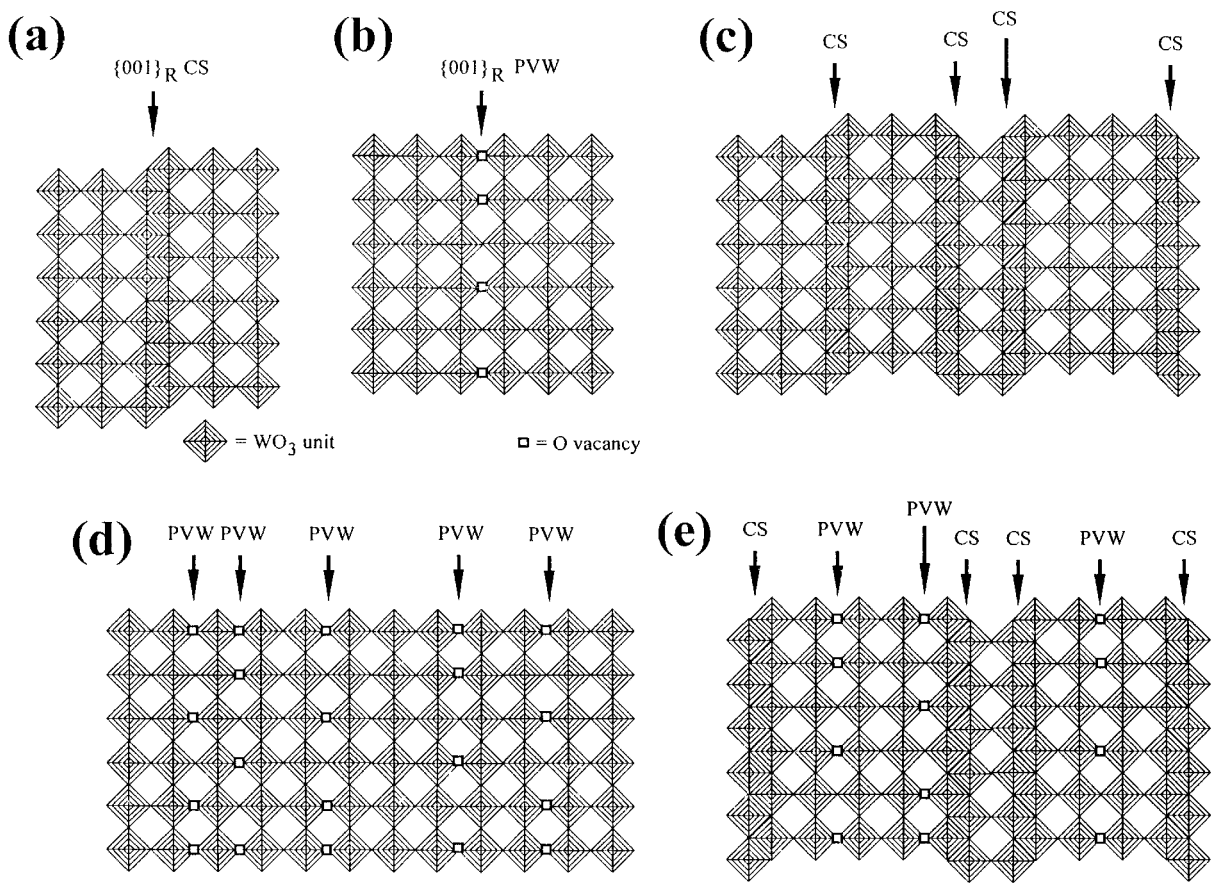

FIG. 13. (a) Depiction of a single $\{001\}_R$ CS plane. (b) Depiction of an individual partial oxygen vacancy wall (PVW). (c) Depiction of randomized CS plane formation interspersed in ReO_3-type lattice. (d) Depiction of randomized PVWs interspersed in an ReO_3-type lattice. (e) Depiction of a random distribution of CS planes and PVWs in an ReO_3-type lattice.

shift to a lower energy (thermodynamic) position will be small relative to that required for its initial formation. The CS plane-by-plane migration route (B(2)) will be limited by similar energy considerations. The mechanisms relying on the formation of additional CS planes or PVWs at thermodynamically favorable loci depend on there already being a partially ordered structure. If it can be shown that the disordered precursors are not partially ordered then this mechanism is not valid. However, the ability of a precursor to form new CS planes (or PVWs) at favorable sites cannot be discounted and, in fact, has already been observed *in situ* (21, 23). In energetic terms, the mechanisms described above that utilize PVW introduction and/or migration are perhaps easier to countenance. However, the main difficulty with establishing these mechanisms is with conclusively demonstrating the existence of PVWs in the precursors. This is difficult as their formation was not directly observed *in situ*, although their possible formation was noted in the case of the precursor oxides (Figs. 4b and 4c; Fig. 5) and in some of the products (Fig. 10b and 11). These observations notwithstanding, the existence of PVWs is difficult to demonstrate by HRTEM imaging alone. However, their inclusion as possible constituent structural elements in the precursor oxides can be justified on both thermodynamic grounds and also in terms of known tungsten oxide chemistry.

Possible thermodynamic justifications for the proposed ordering mechanisms and also the nature of the observed structures can be found in the work of Iguchi and Tilley (36, 37) and Iguchi (38). These authors calculated the strain energy between pairs of $\{10m\}_R$ and $\{100\}_R$ CS planes and thereby demonstrated that the energy for a given composition decreases with increasing m and also that the strain energy for $\{100\}_R$ CS planes is lower in comparison to other types of shear planes. Iguchi further extended these calculations for the $\{001\}_R$ case and calculated that for W_nO_{3n-1} CS structures with values of n from 4 to 63 (with the exception of $n = 22$), the net force between the $\{001\}_R$ CS planes was attractive. The same author also calculated that for W_nO_{3n-1} CS structures with $n < 4$, the net force between the $\{001\}_R$ CS planes was repulsive. This result is apparently

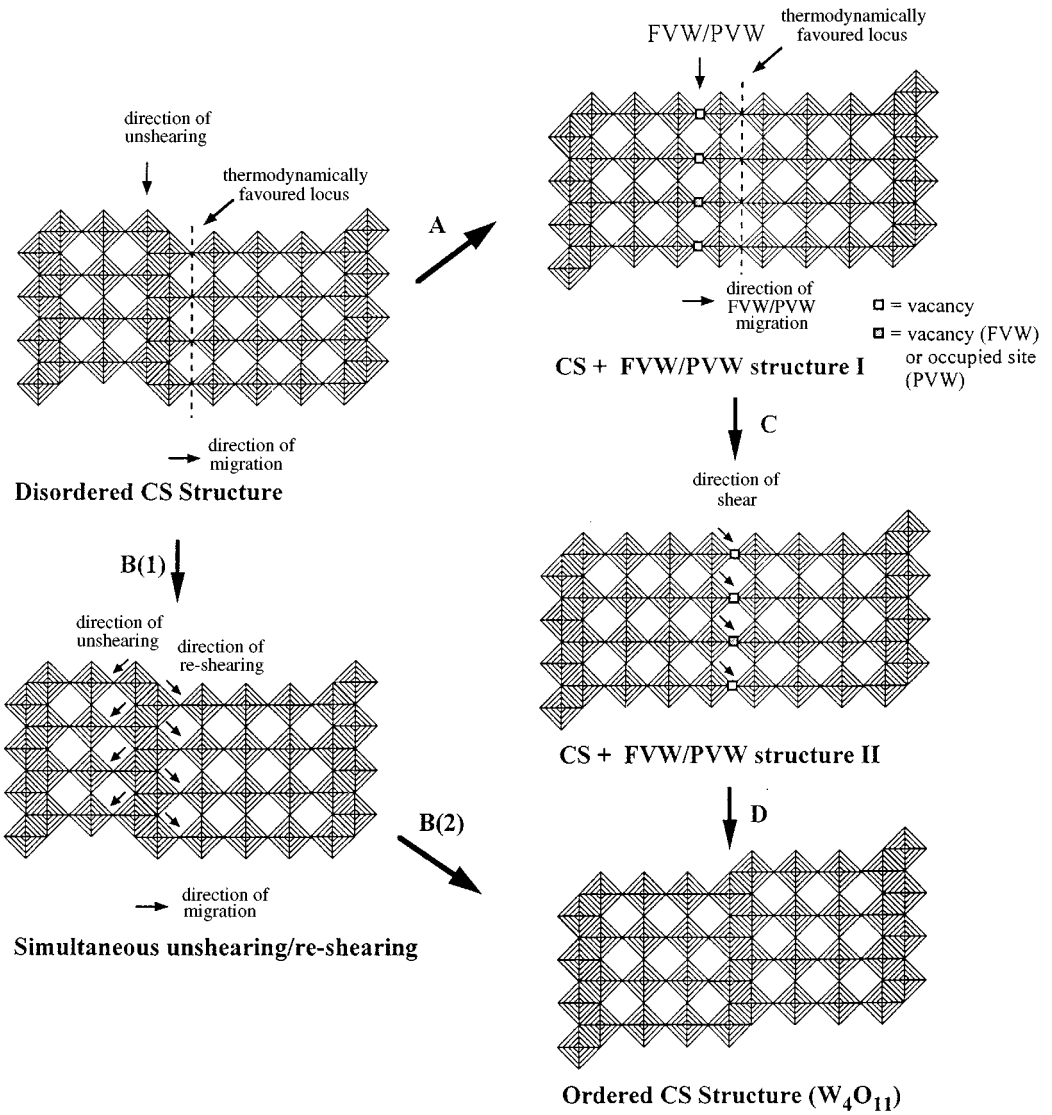

FIG. 14. Schemes showing ordering of CS planes to form W_nO_{3n-1}-type layered structures. (Scheme A) Unshearing of disordered CS structure to form FVW intermediate. This intermediate serves also for the PVW structure (see Fig. 13e). (Scheme B(1 + 2)). Simultaneous shearing followed by migration to form ordered CS structure (W_4O_{11}). (Scheme C) Migration of FVW/PVW to thermodynamically favored locus. (Scheme D). Shearing or FVW/PVW to form ordered CS structure.

in agreement with the expanded $n = 3$ microstructure seen in Fig. 10a. These calculations can also be seen as providing the energetic basis for the observed tendency toward ordering of the encapsulated W_nO_{3n-1} phases described in this study.

One further point is the possible contribution of encapsulation with respect to the process of ordering. It is possible that the existence of the 2H–WX_2 fullerene-like shells around the oxides may contribute in some way to boundary conditions which may be necessary for the ordering process. This can only be verified by the observation of similar ordering to that described in this paper with respect to "free" WO_{3-x} crystals that are not encapsulated within 2H–WX_2 networks.

4.3. Role of Sodium

Most of the encapsulated metal oxides described in this paper were formed in the presence of sodium and XPS studies revealed that Na was present both in the oxide precursors and also in the final encapsulated products. XRD studies indicated that Na was present as an intercalant in the encapsulating 2H–WS_2 layers resulting in ordered superstructures in the encapsulating layered network and this was also found to greatly enhance the dispersability of both the precursors and the encapsulate oxides in aprotic solvents (9). The fact that EDX revealed only very small quantities of Na suggests that this intercalant was not

strongly bound either to the oxide precursors or as an intercalant within the 2H–WS_2 encapsulating network. Further, the observed encapsulated microstructures are not consistent with those typically formed by sodium tungsten oxide compounds. It was shown recently, for example, that Na bronzes of the form Na_xWO_3 ($x = 0.1$) form weak perovskite type superstructures (39). These were not observed in either the precursor oxides or their encapsulated derivatives. Therefore we have interpreted the microstructures of these larger needles in terms of their WO_{3-x} defect microstructures only. However, it is quite possible that Na doping may play some role in stabilizing some of the observed structures, as has been observed with other metal-doped CS-related structures (see, for example, Ekström and Tilley and Ekström *et al.* (40, 41)). We hope to comment more upon this issue and all of the issues raised by the observed ordering of W_nO_{3n-1} oxides within 2H–WX_2 IF-like structures subsequently.

4.4. Conclusions

The encapsulation of complex tungsten oxides, consisting of Wadsley-type defect oxides to complex layered oxides of the form W_nO_{3n-1} inside 2H–WX_2 (X = S and Se) inorganic fullerene-like has been described. The relationships between the oxide precursors, in terms of both their microstructures and morphologies, and the obtained encapsulates has been described in some detail. The phenomenon of ordering with respect to the formation of the ordered and partially ordered encapsulates was also discussed.

Given the wide variety of applications of both the encapsulated oxides and also of their encapsulating chalcogenides, these new hybrid materials are of potentially great technological significance in materials science. A further point is that the choice of metal with respect to the encapsulated complex oxides and their encapsulating dichalcogenides is not necessarily limited to tungsten. In fact, anything that forms a 2H–MX_2-type layered chalcogenide (or similar) can potentially form a complex oxide encapsulate. This means that the complex oxides of transition metals such as Ti, Zr, Hf, V, Nb, Ta, Cr, Mo, and Cr and even main group metals such as Sn can potentially be prepared as encapsulates. Furthermore, combinations of the above and other metals in encapsulated mixed metal oxide formulations may also be anticipated. The surprising and unprecedented nature of these new materials points toward new directions in both encapsulation technology and solid state science.

ACKNOWLEDGMENTS

The authors are indebted to the UK–Israel Science and Technology program for financial support. This program is governed jointly by the British Council and the Israel Ministry of Science.

REFERENCES

1. R. Tenne, L. Margulis, M. Genut, and G. Hodes, *Nature* (*London*), **360,** 444 (1992).
2. L. Margulis, G. Salitra, R. Tenne, and M. Talianker, *Nature* (*London*) **365,** 113 (1992).
3. M. Hershfinkel, L. A. Gheber, V. Volterra, J. L. Hutchison, L. Margulis, and R. Tenne, *J. Am. Chem. Soc.* **116,** 1914 (1994).
4. Y. Feldman, E. Wasserman, D. J. Srolovitz, and R. Tenne, *Science* **267,** 222 (1995).
5. R. Tenne, *Adv. Mater.* **7,** 965 (1995).
6. S. Iijima, *Nature* (*London*) **354,** 56 (1991).
7. L. Margulis, J. L. Hutchison, and R. Tenne, *in* "New Horizons for Materials" (P. Vincenzini, Ed.), pp. 301–308. Techna Sci, 1995.
8. L. Rapoport, Y. Bilik, Y. Feldman, M. Homyonfer, S. R. Cohen, and R. Tenne, *Nature* (*London*) **387,** 791 (1997).
9. M. Homyonfer, B. Alperson, Y. Rosenberg, L. Sapir, S. R. Cohen, G. Hodes, and R. Tenne, *J. Am. Chem. Soc.* **119,** 2693 (1997).
10. Y. Watanabe, *Wear* **155,** 237 (1992).
11. S. G. Deleon, P. Grange, and B. Delmon, *Appl. Catal. A* **107,** 101 (1993).
12. Y. Feldman, G. L. Frey, M. Homyonfer, V. Lyakhovitskaya, L. Margulis, H. Cohen, G. Hodes, J. L. Hutchison, and R. Tenne, *J. Am. Chem. Soc.* **118,** 5362 (1996).
13. A. Magnéli, *Acta Chem. Scand.* **2,** 501 (1948).
14. A. Magnéli, *Ark. Kemi.* **1,** 513 (1950).
15. A. Magnéli, *Ark. Kemi.* **6,** 133 (1953).
16. J. S. Anderson and B. G. Hyde, *J. Phys. Chem. Solids* **28,** 1393 (1967).
17. L. A. Bursill and B. G. Hyde, *J. Solid State Chem.* **4,** 430 (1972).
18. S. Amelinkx and J. van Landuyt, "The Chemistry of Extended Defects in Non-metallic Solids," p. 295, North-Holland, Amsterdam, 1970.
19. M. Sundberg and R. J. D. Tilley, *J. Solid State Chem.* **11,** 150 (1974).
20. R. J. D. Tilley, *Chem. Scr.* **14,** 147 (1979).
21. T. Miyano, M. Iwanishi, C. Kaito, and M. Shiojiri, *Jap. J. Appl. Phys.* **22,** 863 (1983).
22. T. Tsirlina, Y. Feldman, M. Homyonfer, J. Sloan, J. L. Hutchison, and R. Tenne, *Full. Sci. Tech.* **6,** 157 (1998).
23. S. Iijima, *J. Solid State Chem.* **14,** 52 (1975).
24. J. P. Bonnet, S. Horiuchi, and I. Kawada, *J. Crystal Growth* **56,** 633 (1982).
25. P. A. Stadelman, *Ultramicroscopy* **21,** 131 (1987).
26. O. Glemser, J. Weidelt, and F. Freund, *Z. Anorg. Allg. Chem.* **332,** 299 (1964).
27. A. Magnéli, Powder Diffraction File card 5-0386 (ASTM, Philadelphia Pennsylvania).
28. A. Magnéli, Powder Diffraction File card 5-392 (ASTM, Philadelphia Pennsylvania).
29. K. Meisel, *Z. Anorg. Allg. Chem.* **207,** 121 (1932).
30. H. Hashimoto, K. Tanaka, and E. Yoda, *J. Phys. Soc. Jap.* **15,** 1006 (1960).
31. A. Kumao, Y. Fujita, and H. Endo, *Ultramicroscopy* **54,** 201 (1994).
32. Powder Diffraction File card No. 8-327 (ASTM, Philadelphia Pennsylvannia).
33. O. Glemser, H. Sauer, and P. Koenig, *Z. Anorg. Allg. Chem.* **257,** 241 (1948).
34. W. Sahle, *J. Solid State Chem.* **45,** 334 (1982).
35. P. Gadó, *Acta Phys. Hung.* **18,** 111 (1965).
36. E. Iguchi and R. J. D. Tilley, *Phil Trans. R. Soc. London A* **286,** 55 (1977).
37. E. Iguchi and R. J. D. Tilley, *J. Solid State Chem.* **24,** 131 (1978).
38. E. Iguchi, *J. Solid State Chem.* **23,** 231 (1978).
39. S. T. Triantafyllou, P. C. Christidis, and Ch. B. Lioutas, *J. Solid State Chem.* **133,** (1997).
40. T. Ekström and R. J. D. Tilley, *J. Solid State Chem.* **19,** 125 (1976).
41. T. Ekström and R. J. D. Tilley, *J. Solid State Chem.* **43,** 251 (1982).